

# Simulating Heterogeneity within Elastic and Inelastic Discrete Mechanical Models

Jan Raisinger<sup>a</sup>, Qiwei Zhang<sup>b</sup>, John E. Bolander<sup>b</sup>, Jan Eliáš<sup>a,\*</sup>

<sup>a</sup>*Institute of Structural Mechanics, Faculty of Civil Engineering, Brno University of Technology, Brno 60200, Czech Republic*

<sup>b</sup>*Department of Civil and Environmental Engineering, University of California, Davis, CA, United States*

---

## Abstract

The study investigates the elastic and fracture behaviors of discrete, elastically homogeneous models of heterogeneous media. The homogeneity is accomplished either by volumetric-deviatoric decomposition of constitutive function or by an auxiliary stress homogenization method. The elastic parameters of the homogenized material models are randomly varied in space to introduce heterogeneity independently of the geometric properties of the discrete model. Several forms of randomization are investigated using statistical properties of nodal stress oscillations in periodic representative volume elements (RVEs). It is found that the stress oscillations present in discrete models built on heterogeneous geometric structures with standard constitutive models cannot be replicated by randomization of the elastically homogeneous discrete system. The marginal distributions as well as dependencies between stress tensor components cannot be adequately matched.

With respect to quasi-brittle fracture behavior, the macroscopic response of the different models is studied for the load case of uniaxial tension. The elastically homogenized material provides higher peak stress occurring at lower strain levels and a steeper softening phase, compared to the standard material. Randomization of the elastic material parameters, as well as adjustment of inelastic material parameters, brings the macroscopic response of the homogenized material close to that of the standard material, although the damage distribution prior to the strain localization differs. These findings provide insight into the potential for controlled, random assignment of heterogeneity in homogeneous models, using physically-based discretizations of material structure with standard constitutive models for comparison.

**Keywords:** concrete; mesoscale; randomness; heterogeneity; stress oscillations; lattice model

---



---

\*Corresponding author, jan.elias@vut.cz

$A$ contact area	$\mathbf{u}$ displacement vector
$\mathbf{c}$ vector from particle node to integration point	$V$ rigid-body volume
$\mathbf{C}$ covariance matrix	$\mathbf{x}$ coordinates in global ref. system
$d$ damage scalar	$\alpha$ contact elastic parameter
$\mathbf{e}$ strain vector	$\boldsymbol{\varepsilon}$ macroscopic strain vector
$\hat{\mathbf{e}}$ vector of eigenstrain	$\boldsymbol{\mathcal{E}}$ Levi-Civita tensor
$E$ macroscopic elastic modulus	$\varepsilon_V$ volumetric strain
$E_0$ contact elastic parameter	$\boldsymbol{\theta}$ rotation vector
$\mathbf{f}$ external forces	$\boldsymbol{\lambda}$ vector of eigenvalues
$f_{\text{eq}}$ elastic limit in given straining direction	$\nu$ macroscopic Poisson's ratio
$f_t$ tensile strength at mesoscale	$\boldsymbol{\xi}$ vector of independent random number from standard normal dist.
$G_t$ mesoscale fracture energy in tension	$\boldsymbol{\sigma}$ stress tensor
$\hat{\mathbf{I}}$ projection tensor	$\chi$ constitutive history variable
$l$ contact length	$\boldsymbol{\psi}$ matrix of eigenvectors
$\mathbf{n}$ unit vector of normal reference system	
$\mathbf{t}$ traction vector	

## 1. Introduction

Discrete models, particularly particle-based lattice models, have been successful in modelling the complex fracture behavior of concrete and other materials with heterogeneous microstructures. There are many types of these models, starting from classical regular and irregular lattice models [45, 44, 57] and early particle-based models [6, 28, 9, 39], up to modern discrete systems with complex constitutive features [37, 34, 24, 25]. The most prominent of them is arguably the Lattice Discrete Particle Model (LDPM), which has been successfully used for various structural configurations and loading scenarios [11, 7, 58]. Nowadays, discrete mechanical models are often coupled with other physical or chemical phenomena [36, 35, 55].

In contrast to continuum descriptions of material behavior, most particle-based discrete models use vectorial constitutive relations defined at the contacts between neighboring particles, which are assumed to be rigid. The heterogeneous geometry and vectorial constitutive functions give rise to local stress oscillations [56] that can be considered beneficial or unfavorable, depending on whether one believes they reflect the stress oscillations in actual materials.

Tessellation of the domain into rigid bodies can be either (i) based on the actual or virtual heterogeneity of the material or (ii) done arbitrarily without consideration of material features. The former approach, called

*physical* discretization in Ref. [8], may be considered as the standard way of building these models. The stress oscillations are then viewed as an advantage allowing, for example, to realistically simulate the failure of concrete under compression [10], which for some applications is an essential capability. Unfortunately, this standard modeling way restricts the range of possible values of macroscopic Poisson’s ratio [16]. The latter, *non-physical* tessellation concept is a discretization technique for which the stress oscillations due to mesh geometry become inappropriate. Two main approaches, the volumetric-deviatoric decomposition of the constitutive functions [12] and auxiliary stress projection method [3, 2], have been developed to eliminate the stress heterogeneity and accurately control the macroscopic Poisson’s ratio. Both approaches exploit information from the neighborhood of a given nodal site, differing from classical lattice models that involve only two node interactions. The resulting material is elastically homogeneous, which can be beneficial when modeling the individual phases or fine-grained matrices of cement-based composite materials [26], for example. However, the complexity of the model response and its ability to represent heterogeneous media are impaired. The material heterogeneity shall be reinstated by some form of randomization, which can be advantageously controlled independently of the discretization strategy. Zhang et al. [56] introduced basic forms of heterogeneity in a controlled manner for elastic stress analysis. The present article describes different forms of randomization, their properties, and potential implications for both elastic and fracture analyses.

When attempting to control material heterogeneity via randomization states, an important question arises: Is it possible to recover the elastic stress oscillations produced by the standard discrete system with *physical* discretization? Since such stress oscillations influence fracture behavior, a large portion of this text is devoted to answering this fundamental question.

Beyond the elastic behavior, the implications of randomizing previously homogeneous systems are studied also in crack development. The randomized models calibrated in the elastic regime are used to simulate fracture behavior due to uniaxial tensile loading. The influence of randomization properties on the macroscopic inelastic response is examined. Once again, the focus is placed on replicating the results obtained by the standard model used with *physical* discretization.

## 2. Modeling framework

The three-dimensional discrete models considered herein are built at the meso-scale, where the aggregate inclusions and cementitious binder are viewed as distinct phases of the composite material. Spherical aggregates are generated according to a specified volume fraction and size distribution, based on a Fuller

sieve curve [54]. The aggregates are then randomly placed into the domain, starting from the largest, prohibiting any overlaps. The modified Delaunay triangulation and power (or Laguerre) tessellations [41] are then generated on the aggregate centroids. The Delaunay simplices provide an estimation of volumetric deformation,  $\varepsilon_V$ , which is one-third of the change of the simplex volume [11]. The power tessellation constitutes rigid bodies representing aggregates and the surrounding matrix, as shown in Fig. 1.

The contacts between rigid bodies are called elements hereinafter, and it will be assumed they always connect nodes  $I$  and  $J$ . They have area  $A$  and length  $l$ , the power tessellation ensures the contact plane is perpendicular to the branch vector connecting nodes  $I$  and  $J$ . The local reference system is given by orthonormal vectors  $\mathbf{n}_N$  (perpendicular to the contact plane),  $\mathbf{n}_M$ , and  $\mathbf{n}_L$ .

Degrees of freedom of the model are the components of displacement,  $\mathbf{u}$ , and rotation,  $\boldsymbol{\theta}$ , vectors defined at each node  $I$ . Assuming small displacement and rotations, the strain vector for each element is given by the following kinematic equation

$$e_\alpha = \frac{1}{l} [\mathbf{u}_J - \mathbf{u}_I + \boldsymbol{\mathcal{E}} : (\boldsymbol{\theta}_J \otimes \mathbf{c}_J - \boldsymbol{\theta}_I \otimes \mathbf{c}_I)] \cdot \mathbf{n}_\alpha \quad (1)$$

where  $\mathcal{E}_{ijk}$  is the Levi-Civita permutation tensor of third order, index  $\alpha \in N, M, L$  refers to the directions in the local reference system, and  $\mathbf{c}_I$  is a vector pointing from node  $I$  to the point  $\mathbf{c}$  (see Fig. 1) where the equation is evaluated. Hereafter, there will be only one such integration point per facet, located at the facet centroid.

The balances of linear and angular momentum for each body  $I$  in steady state are expressed as

$$\sum_{\alpha} \sum_{e \in I} A_e t_{\alpha}^e \mathbf{n}_{\alpha}^e = \mathbf{0} \quad \sum_{\alpha} \sum_{e \in I} A_e t_{\alpha}^e \boldsymbol{\mathcal{E}} : \mathbf{c}_I^e \otimes \mathbf{n}_{\alpha}^e = \mathbf{0} \quad (2)$$

The first of these equations sums tractions,  $\mathbf{t}$ , acting at each element  $e$  attached to node  $I$ ; the second equation sums moments of those tractions with respect to node  $I$ . In the presence of body forces, body couples, couple tractions or in a transient regime, additional terms must be included.

The modeling framework is completed by a constitutive equation. Several variants of the constitutive model are examined in this paper, as described in the following sections.

### 2.1. Elastic constitutive equations

**Variant S:** The standard constitutive model has two material parameters,  $E_0$  and  $\alpha$ . The traction



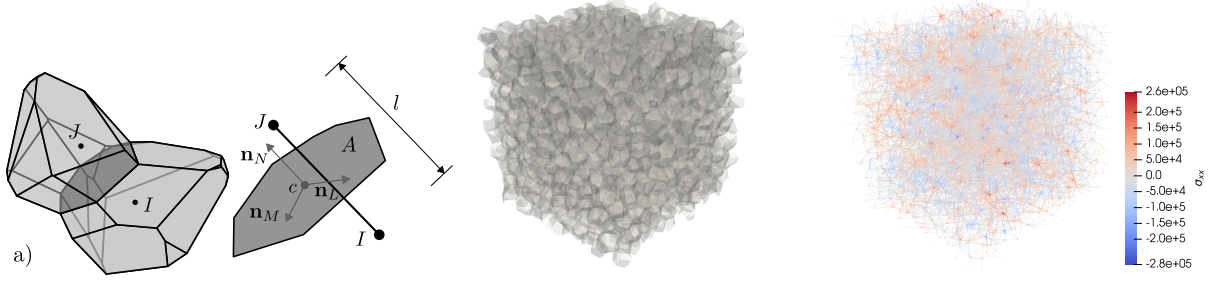


Figure 1: a) Two rigid bodies connected by element of length  $l$ , area  $A$ , and local reference system  $\mathbf{n}_\alpha$ ,  $\alpha \in \{N, M, L\}$ ; b) periodic set of contact facets in an RVE of size  $l_{\text{RVE}} = 100$  mm; c) discrete elements of the same RVE colored by  $\sigma_{xx}$  component of nodal stress under pure shear strain load.

components are

$$t_N = E_0 e_N \quad t_M = \alpha E_0 e_M \quad t_L = \alpha E_0 e_L \quad (3)$$

The  $\alpha$  parameter is responsible for macroscopic Poisson's ratio, see, e.g., Refs. [5, 30]. This is the most commonly used constitutive model, which results in local oscillations of macroscopic stress in the model [56]. Hereinafter, we will denote this standard constitutive model by letter *S*. The *approximate* relations of  $E_0$  and  $\alpha$  to the macroscopic elastic parameters  $E$  (Young's modulus) and  $\nu$  (Poisson's ratio), derived from Voigt's kinematic assumption, are

$$\nu \approx \frac{1 - \alpha}{4 + \alpha} \quad E \approx E_0 \frac{2 + 3\alpha}{4 + \alpha} \quad (4)$$

**Variant V:** To have better control over Poisson's ratio and to avoid the stress oscillations, Cusatis, Rezakhani, and Schaufert [12] developed a constitutive model featuring material elastic constants  $E_V$  and  $E_D$  with constitutive relations

$$t_N = E_D e_N + (E_V - E_D) \varepsilon_V \quad t_M = \alpha E_D e_M \quad t_L = E_D e_L \quad (5)$$

Each contact has several simplices attached to it (as many as the number of vertices of the contact facet), so the volumetric strain  $\varepsilon_V$  is obtained as an average from those attached simplices. Because the element formulation in our numerical implementation involves only the degrees of freedom of the two nodes,  $I$  and  $J$ , the volumetric strain must be supplied from outside and the contact stiffness matrix does not have the effect of the volumetric strain included. This means that, even for linear elasticity, this implementation of the constitutive model requires iteration toward meeting the convergence criteria in each time step. This

constitutive model will be denoted as  $\mathbf{V}$  in the following text.

The *exact* relations between the  $E_D$  and  $E_V$  material parameters and macroscopic elastic modulus and Poisson's ratio read [12]

$$E = \frac{3E_VE_D}{E_D + 2E_V} \quad \nu = \frac{E_V - E_D}{E_D + 2E_V} \quad (6a)$$

$$E_D = \frac{E}{1 + \nu} \quad E_V = \frac{E}{1 - 2\nu} \quad (6b)$$

**Variante H:** The third constitutive model, developed in Refs. [3, 2], follows the standard model from Eq. (3) with  $\alpha = 1$ . The parameter  $E_0$  is then directly equal to the macroscopic elastic modulus (i.e.,  $E_0 = E$ ) and the macroscopic Poisson's ratio is 0. Moreover, by setting  $\alpha = 1$ , the discrete model does not exhibit any stress oscillation. In other words, the model is elastically homogeneous, as shown by the proof in Refs. [15, 16, 56]. The macroscopic stress tensor can be estimated in each rigid body  $I$  by the Love-Weber formula [33, 52, 13, 29, 4, 18]

$$\boldsymbol{\sigma}_I = \frac{1}{V_I} \sum_f \mathbf{x}_f \otimes \mathbf{f}_f = \frac{1}{V_I} \sum_{\alpha} \sum_{e \in I} A_e t_{\alpha} \mathbf{c}_{eI} \otimes \mathbf{n}_{\alpha}^e \quad (7)$$

where the first summation runs over all external forces  $\mathbf{f}_f$  acting at position  $\mathbf{x}_f$ , and the second summation acknowledges that these external forces are associated with adjoining elements  $e$  for which the contact force becomes  $\mathbf{f}_f = A_e t_{\alpha} \mathbf{n}_{\alpha}$ , vector  $\mathbf{c}_{eI}$  connects the facet centroids with governing node of the particle, and  $V_I$  is volume of the rigid body. The stress tensor is symmetric unless a volume couple or couple traction at the contact facets is applied [40, 53].

After the macroscopic stress for each particle is evaluated, the average tensorial stress in the contact element  $IJ$  is evaluated as  $\bar{\boldsymbol{\sigma}}_{IJ} = 0.5(\boldsymbol{\sigma}_I + \boldsymbol{\sigma}_J)$ . Its eigen decomposition reads  $\bar{\boldsymbol{\sigma}}_{IJ} = \boldsymbol{\Psi}_{IJ} \text{diag}(\boldsymbol{\lambda}_{IJ}) \boldsymbol{\Psi}_{IJ}^T$  with eigenvectors collected in columns of tensor  $\boldsymbol{\Psi}_{IJ}$  and principal stresses in vector  $\boldsymbol{\lambda}_{IJ}$ , the  $\text{diag}(\bullet)$  operation transforms the vector into diagonal matrix. This decomposition is projected into eigenstrains  $\hat{\mathbf{e}}_{IJ}$  of the element using a projection tensor  $\hat{\mathbf{I}}$  [3, 2]

$$\hat{\mathbf{e}}_{\alpha}^{IJ} = \frac{\nu}{E} \mathbf{n}_{\alpha}^{IJ} \cdot \boldsymbol{\Psi}_{IJ} \cdot \text{diag} \left( \hat{\mathbf{I}} \cdot \boldsymbol{\lambda}_{IJ} \right) \cdot \boldsymbol{\Psi}_{IJ}^T \cdot \mathbf{n}_N^{IJ} \quad \text{where} \quad \hat{\mathbf{I}} = \begin{pmatrix} 0 & 1 & 1 \\ 1 & 0 & 1 \\ 1 & 1 & 0 \end{pmatrix} \quad (8)$$

The eigenstrains modify tractions, which enter Eq. (8) again. An iterative loop searching for global balance

is applied until the convergence criterion is met. The resulting solution exhibits macroscopic Poisson's ratio and Young's modulus *exactly* equal to  $\nu$  and  $E$  inserted in Eq. (8).

Notice that the V and H variants produce essentially the same elastically homogeneous model, differing only in the parameters controlling them. In both cases, the resulting medium locally and globally corresponds to a homogeneous material with identical macroscopic parameters.

## 2.2. Inelastic constitutive equations

The elastic constitutive models in variants S and H are extended into inelastic behavior using the damage parameter  $d$

$$t_N = (1 - d)E_0 (e_N - \hat{e}_N) \quad t_M = (1 - d)E_0\alpha (e_M - \hat{e}_M) \quad t_L = (1 - d)E_0 (e_L - \hat{e}_L) \quad (9)$$

where eigenstrain  $\hat{e}_\alpha$  is given by Eq. (8) for variant H and is zero for variant S.

The damage parameter is evaluated in space of equivalent strain,  $e_{\text{eq}}$ , and equivalent traction,  $t_{\text{eq}}$ , as

$$d = 1 - \frac{t_{\text{eq}}}{E_0 e_{\text{eq}}} \quad (10)$$

where

$$e_{\text{eq}} = \sqrt{e_N^2 + \alpha e_T^2} \quad e_T = \sqrt{e_M^2 + e_L^2} \quad t_{\text{eq}} = f_{\text{eq}} \exp \left( \frac{K}{f_{\text{eq}}} \left\langle \chi - \frac{f_{\text{eq}}}{E_0} \right\rangle \right) \quad (11)$$

The angled brackets return the positive part of the argument. The direction-dependent strength,  $f_{\text{eq}}$ , initial

slope of softening/hardening,  $K$ , and history variable,  $\chi$ , are

$$f_{\text{eq}} = \begin{cases} \frac{16f_t}{\sqrt{\sin^2 \omega + \alpha \cos^2 \omega}} & \omega < \omega_0 \\ f_t \frac{4.52 \sin \omega - \sqrt{20.07 \sin^2 \omega + 9\alpha \cos^2 \omega}}{0.04 \sin^2 \omega - \alpha \cos^2 \omega} & \omega \geq \omega_0 \end{cases} \quad (12a)$$

$$K = \begin{cases} 0.26E_0 \left[ 1 - \left( \frac{\omega + \pi/2}{\omega_0 + \pi/2} \right)^2 \right] & \omega < \omega_0 \\ -K_t \left[ 1 - \left( \frac{\omega - \pi/2}{\omega_0 - \pi/2} \right)^{n_t} \right] & \omega \geq \omega_0 \end{cases} \quad (12b)$$

$$\chi = \begin{cases} e_{\text{eq}} & \omega < \omega_0 \\ e_{\text{eq}} \frac{\omega}{\omega_0} + \sqrt{\max e_N^2 + \alpha \max e_T^2} \left( 1 - \frac{\omega}{\omega_0} \right) & \omega_0 \leq \omega < 0 \\ \sqrt{\max e_N^2 + \alpha \max e_T^2} & \omega \geq 0 \end{cases} \quad (12c)$$

Parameter  $\omega$  expresses straining direction,  $\tan \omega = e_N / \sqrt{\alpha} e_T$ , and  $\omega_0$  is the direction at which both branches of Eq. (12a) are equal. History variables  $\max e_N^2$  and  $\max e_T^2$  represent maximum square normal and shear strain achieved from the beginning of the simulation. The initial slope of the strain softening,  $K$ , is defined using  $K_t$  and  $K_s$ , the slopes for pure tension and shear, respectively. These are dependent on contact length  $l$  and read

$$K_t = \frac{2E_0 f_t^2 l}{2E_0 G_t - f_t^2 l} \quad K_s = \frac{18\alpha E_0 f_t^2 l}{32\alpha E_0 G_t - 9f_t^2 l} \quad (13)$$

Finally, parameter  $n_t$  reads

$$n_t = \frac{\ln(K_t / (K_t - K_s))}{\ln(1 - 2\omega_0 / \pi)} \quad (14)$$

The presented constitutive model is based on a formulation developed in Ref. [10], which was a predecessor of the Lattice-Discrete Particle Model [11, 1]. It is largely modified by omitting the confinement effect, using damage parameter in shear and compression, and reducing number of material parameters to four: normal elastic constant  $E_0$ , tangential/normal stiffness ratio  $\alpha$ , tensile strength  $f_t$  and tensile fracture energy  $G_t$ . The model has been validated using experimental data from cases dominated by tensile fracture [22, 14, 19]. It has not been optimized and validated for compression.

### 2.3. Model geometry and periodic boundary conditions

The model is generated with periodic geometry in a cube of size  $l_{\text{RVE}}$ , called Representative Volume Element (RVE) hereinafter. Firstly, the Fuller curve is used to generate spheres of diameters within range 4 to 10 mm [54]. These spheres are placed randomly into the domain without overlapping, starting from the largest diameter spheres. The Euclidean metric used to check whether the overlapping is periodic, i.e., distance between two points  $I$  and  $J$  along axis  $i$  is  $\Delta x_i = \min(|x_i^J - x_i^I|, 0.5l_{\text{RVE}} - |x_i^J - x_i^I|)$  [20, 50]. Then, the periodic power tessellation is performed. The periodicity is enforced by periodic repetition of the particles close to the domain boundary, see, e.g., Ref. [21] where the same strategy is used for Voronoi tessellation. The main advantage of the fully periodic geometry is complete elimination of all boundary effects described in Ref. [15]. An example of a periodic RVE is presented in Fig. 1b.

The boundary conditions applied to the model are periodic as well. There is a prescribed macroscopic strain tensor,  $\boldsymbol{\varepsilon}$ , that drives the difference of displacements of the primary ( $I$ ) and dependent ( $J$ ) nodes at the surface of the periodic structure

$$\mathbf{u}_J = \mathbf{u}_I + (\mathbf{x}_J - \mathbf{x}_I) \cdot \boldsymbol{\varepsilon} \qquad \boldsymbol{\theta}_J = \boldsymbol{\theta}_I \qquad (15)$$

To prevent rigid-body translations, one node is randomly selected and its displacements are restricted. Rigid-body rotations are automatically prevented by the period boundary conditions. The applied loading differs from the one derived by asymptotic homogenization in Refs. [42, 43, 17], which features projection of the macroscopic strain tensor into eigenstrains in discrete contact elements. The loading through eigenstrains is replaced for the sake of simplicity because the eigenstrains are already used to introduce the Poisson's effect in Eq. (8). If needed, both eigenstrain sources can be used simultaneously, but the direct loading through Eq. (15) provides exactly identical results and its description in connection with Eq. (8) seems less complicated.

Periodic models of size  $l_{\text{RVE}} = 100$  mm are used for the elastic analysis and size  $l_{\text{RVE}} = 50$  mm for the inelastic analysis. A set of 100 models differing by internal geometry is generated for each RVE size. On average each model of size  $l_{\text{RVE}} = 100$  mm contains about 19900 elements and 3400 nodes. In the inelastic analyses, stress field oscillations are not inspected; only the global response character is examined. The smaller size models were used with the advantage of significantly faster computation times.

All the simulations are performed in the open-source software OAS (Open Academic Solver) available at <https://gitlab.com/kelidas/OAS>. This software is developed at Brno University of Technology as

a multipurpose platform for the solution of various physical problems. The simulations are computed as steady state using a modified Newton-Raphson iteration scheme.

### 3. Linear elastic material behavior

The first investigation is directed towards elastic behavior. The following material variants and parameters are used.

- **Variant S**, the standard material with material parameters  $E_0 = 40 \text{ GPa}$  and  $\alpha = 0.24$ , values typically used for ordinary concrete. For further analysis, effective macroscopic elastic modulus,  $E_{\text{eff}}$ , and effective macroscopic Poisson's ratio,  $\nu_{\text{eff}}$ , is found for each RVE. An effective macroscopic stiffness tensor is constructed by loading each RVE by strain in six linearly independent directions (three normal and three shear loads). Effective  $E$  and  $\nu$  values are found by numerical fitting of the theoretical isotropic stiffness tensor to this computed tensor.

The choice of the elastic modulus is not important, it only linearly scales the results. However, the value of  $\alpha$  affects the stress oscillations. For  $\alpha = 1$ , the stress oscillations completely disappear, see, e.g., Ref. [16, 56].

- **Variant V** with the volumetric-deviatoric split uses the effective parameters from the S variant in Eq. (6b) for each RVE internal geometry:  $E_D = E_{\text{eff}}/(1 + \nu_{\text{eff}})$  and  $E_V = E_{\text{eff}}/(1 - 2\nu_{\text{eff}})$ . The randomized version of this material variant applies randomness only to the deviatoric part.

- **Subvariant V-RD** has parameter  $E_D$  randomly drawn from a uniform distribution with user-defined width. The width is specified by parameter  $\eta$  determining the lower bound as  $(1 - \eta)\mu_D$  and the upper bound as  $(1 + \eta)\mu_D$  where  $\mu_D$  is the mean value. The mean value of the uniform distribution is set so each RVE stiffness with V-RD material matches the stiffness of the same RVE geometry with S material, i.e., each RVE geometry uses distribution with slightly different mean value. The reason why the randomization changes the means value, apart from not large enough statistical sample, is simply the interaction between elastic contacts. In an extreme case of all contacts connected in series, the elastic modulus would read  $E = (\sum_i 1/E_i)^{-1}$ . In another extreme case of parallel connectivity, the elastic modulus would read  $E = \sum_i E_i$ . The complex structure of the RVE gives values between those extremes. Both the mean of  $E_D$  and the deterministic value of  $E_V$  are modified so the V-RD RVE stiffness tensor matches the S RVE stiffness tensor.

- **Variant H**, a material homogenized by projection of tensorial stresses, with parameters  $E = E_{\text{eff}}$  and  $\nu = \nu_{\text{eff}}$ . These parameters are, as in the case of V variant, different for each RVE geometry so the stiffness of each RVE with H material matches the stiffness calculated for S material. These elastic parameters of each element are also randomized by one of the following approaches.

- **Subvariant H-R** assumes both  $E$  and  $\nu$  uniformly distributed and independent, and without any spatial correlation. In other words,  $E$  and  $\nu$  for each element are drawn independently from uniform distributions with mean values  $\mu_E$  and  $\mu_\nu$  and width parameters  $\eta_E$  and  $\eta_\nu$ . The meaning of the width parameters is identical to the one in V-RD variant and they are specified by the model user. Since the mean values for each randomized RVE are computed in the same way as for V-RD variant, the stiffness tensor must match the stiffness tensor of the RVE with standard (S) material.
- **Subvariant H-RD** randomizes only the deviatoric component of the material stiffness,  $E_D$ , while keeping the volumetric part constant. For each element the parameter  $E_D$  is drawn from a uniform distribution and values of elastic modulus and Poisson's ratio are then calculated from Eq. (6a). The width parameter  $\eta_D$  is a free model parameter while its mean value and constant  $E_V$  are updated as in all the previous random models so stiffness of each randomized RVE corresponds to stiffness of the RVE with the standard (S) material.
- **Subvariant H-RF** employs independent  $E$  and  $\nu$  generated as realizations of random fields with uniform marginal distributions. The uniform distribution has user-defined widths (through  $\eta$  parameters) and mean values correspond to the mean effective values from all 100 RVEs with the standard (S) material. The Gaussian (square exponential) autocorrelation function is used and the correlation length  $\ell_c$  is another user-defined material parameter.

Random fields are generated via the Karhunen–Loève expansion [27, 46, 47, 23]. It is based on the spectral decomposition of covariance matrix  $\mathbf{C}$ , which transforms the correlated Gaussian variables into independent standard Gaussian variables, which are simple to generate. The covariance matrix  $\mathbf{C}$  is computed with the help of the periodic metric [20, 50] so the resulting field is periodic as well. The periodic Gaussian random field is obtained using vector  $\boldsymbol{\xi}$  of  $K$  standard Gaussian random variables

$$\hat{H}(\mathbf{x}) = \sum_{k=1}^K \sqrt{\lambda_k} \xi_k \boldsymbol{\psi}_k(\mathbf{x}) \quad (16)$$

where  $\lambda$  and  $\boldsymbol{\psi}$  are the eigenvalues and the eigenvectors of the covariance matrix  $\mathbf{C}$ , and  $K$  is the number of eigenmodes considered. Only  $K$  eigenmodes corresponding to  $K$  largest eigenvalues are used, so that  $\sum_{k=1}^K \lambda_k$  is at least 99 % of the trace of the covariance matrix  $\mathbf{C}$  [48]. The independent standard Gaussian variables  $\boldsymbol{\xi}$  must be sampled carefully. Ideally, one should use Latin Hypercube Sampling and some robust optimization strategy allowing optimal integration properties of the resulting set [51, 20, 50].

The Gaussian field is generated on a grid and then projected onto the discrete mechanical structure by the expansion-optimal linear estimation method (EOLE) developed by Li and Der Kiureghian [31]), see papers [22, 19] which apply the identical strategy.

After the Gaussian random field values at facet centers are obtained, they are transformed to non-Gaussian space using isoprobabilistic transformation. This transformation distorts the correlations, therefore when generating the underlying Gaussian field in Eq. (16), the correlation coefficients in matrix  $\mathbf{C}$  must be modified in order to fulfill the desired pairwise correlations of the non-Gaussian field. This is provided by the Nataf model, which can be evaluated by an approximation from Ref. [32].

One can randomize the variant  $\mathbf{V}$  in a different way (using random fields, randomizing also  $E_V$  parameter, or randomize some combination of  $E_V$  and  $E_D$ , for example as done in H-R by independent randomization of  $E$  and  $\nu$ ). As discussed earlier, variants  $\mathbf{V}$  and  $\mathbf{H}$  are essentially identical, differing only in the way macroscopic material properties are assigned. The other randomization variants of  $\mathbf{V}$  material would therefore only revisit the  $\mathbf{H}$  material randomization. However, in the  $\mathbf{H}$  variant the application of the spatial randomness is blended with computing the average stress tensor in the rigid bodies. In the  $\mathbf{V}$  variant, it is applied directly to the element. That is the primary reason why variant  $\mathbf{V}$ -RD is introduced. It can be directly compared to  $\mathbf{H}$ -RD variant to observe how different forms of introducing the same form of randomness affect the results.

In all the random models only uniform distribution is used. Other distributions can be easily inserted instead. Also, one can study the effect of the relationship between random values of the two elastic parameters, so-called cross correlation. These options are not investigated in the present study but shall be addressed in the future.

The RVEs of size  $l_{\text{RVE}} = 100 \text{ mm}$  with different variants of elastic constitutive models are subjected to macroscopic strain loading. The tensorial stresses are evaluated by Eq. (7) for the node of each rigid body. Due to perfect periodicity of the whole model, the ergodicity of the stress field is ensured and statistical sampling in space and over RVE realizations is equivalent. A statistical assessment is presented for different



load	$\{\varepsilon_{xx}, \varepsilon_{yy}, \varepsilon_{zz}, \varepsilon_{yz}, \varepsilon_{xz}, \varepsilon_{xy}\} (\times 10^{-5})$	$\varepsilon_{\text{dev}} (\times 10^{-5})$	$\varepsilon_V (\times 10^{-5})$	$\varepsilon_{\text{eq}} (\times 10^{-5})$
1	$\{1.5, 1.5, 1.5, 0, 0, 0\}$	$\{0, 0, 0, 0, 0, 0\}$	1.5	0
2	$\{0, 0, 0, 1.50, 1.50, 1.50\}$	$\{0, 0, 0, 1.50, 1.50, 1.50\}$	0.0	4.50
3	$\{0, 0, 0, 0, 0, 2.60\}$	$\{0, 0, 0, 0, 0, 2.60\}$	0.0	4.49
4	$\{1.5, 1.5, 1.5, 0, 0, 2.60\}$	$\{0, 0, 0, 0, 0, 2.60\}$	1.5	4.49

Table 1: Applied strains for elastic analysis

material variant		$\sigma_{xx}/\sigma_V$	$\sigma_{yy}/\sigma_V$	$\sigma_{zz}/\sigma_V$	$\sigma_{yz}/\sigma_V$	$\sigma_{xz}/\sigma_V$	$\sigma_{xy}/\sigma_V$
S	average	1.000	1.000	1.000	$\sim 10^{-22}$	$\sim 10^{-22}$	$\sim 10^{-22}$
	stand. dev.	$\sim 10^{-20}$	$\sim 10^{-20}$	$\sim 10^{-20}$	$\sim 10^{-20}$	$\sim 10^{-20}$	$\sim 10^{-20}$
H	average	1.000	1.000	1.000	$\sim 10^{-16}$	$\sim 10^{-16}$	$\sim 10^{-16}$
	stand. dev.	$\sim 10^{-14}$	$\sim 10^{-14}$	$\sim 10^{-14}$	$\sim 10^{-14}$	$\sim 10^{-14}$	$\sim 10^{-14}$
H-R	average	1.000	1.000	1.002	$\sim 10^{-10}$	$\sim 10^{-10}$	$\sim 10^{-10}$
	stand. dev.	0.105	0.105	0.103	0.053	0.053	0.053
H-RD	average	1.000	1.000	1.000	$\sim 10^{-14}$	$\sim 10^{-14}$	$\sim 10^{-14}$
	stand. dev.	$\sim 10^{-13}$	$\sim 10^{-13}$	$\sim 10^{-13}$	$\sim 10^{-14}$	$\sim 10^{-14}$	$\sim 10^{-14}$
V-RD	average	1.000	1.000	1.002	$\sim 10^{-10}$	$\sim 10^{-10}$	$\sim 10^{-10}$
	stand. dev.	$\sim 10^{-13}$	$\sim 10^{-13}$	$\sim 10^{-13}$	$\sim 10^{-13}$	$\sim 10^{-13}$	$\sim 10^{-13}$

Table 2: Averages and standard deviations of stress field components produced by volumetric *Load 1*,  $\varepsilon_V = 1.5 \times 10^{-5}$  acting on 100 RVEs. The average and standard deviation values have been normalized by the theoretical value of volumetric stress  $\sigma_V = E_V \varepsilon_V = 0.600$  MPa. The width parameters are  $\eta_E = \eta_\nu = 0.95$  for H-R material and  $\eta_D = 0.8$  for H-RD and V-RD materials.

loading scenarios: (i) volumetric loading, (ii) deviatoric loading, and (iii) general loading composed of both volumetric and deviatoric parts. The strain loading tensors are listed in Tab. 1. For each case, 100 RVEs with different internal structures and different random values of material parameters (if applied) are included in the analysis.

### 3.1. Volumetric strain load

The imposed macroscopic strain tensor, denoted as *Load 1*, reads  $\varepsilon_{ij} = \varepsilon_V \delta_{ij}$ , where  $\delta_{ij}$  is Kronecker delta and  $\varepsilon_V$  is a scalar representing volumetric strain.  $\varepsilon_V$  is chosen to be  $1.5 \times 10^{-5}$  without loss of generality as any other value would produce identical results only multiplied by appropriate constant.

As documented in Tab. 2, the tensorial stress field produced by the standard material (S) is constant for all rigid bodies within machine precision. The resulting stress is hydrostatic, the normal components are identical and there are no shear stresses. The standard deviations of all the components are practically zero. The very same is seen for H material variant, except this time the variances are higher as the iterative procedure stopped at some threshold and therefore introduced random numerical error into the solution. Lowering the convergence limit would decrease the variances but also demand more computational resources.

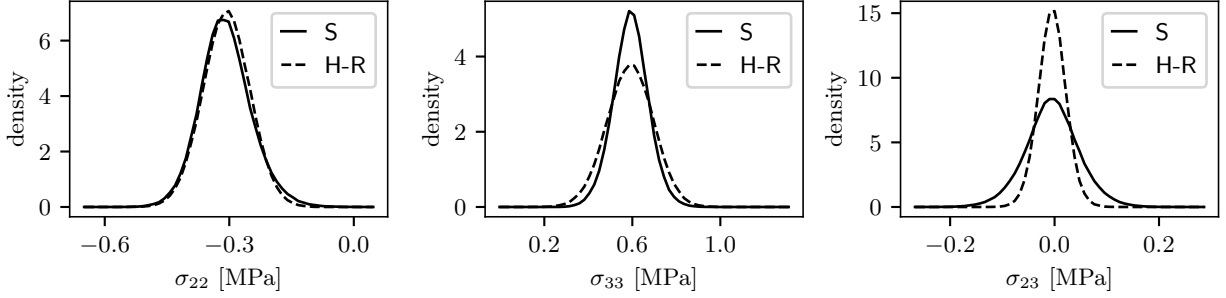


Figure 2: Examples of histogram differences  $\Delta_{\text{hist}}$  between S and H-R material variants computed on RVEs subjected to *Load 2*: from the left  $\Delta_{\text{hist}} = 1.723$ ;  $-2.970$ ;  $14.234$ .

The results for V material variant are not reported in the table but they are identical to the H variant. These models are, in the deterministic setup, indistinguishable.

Further rows in Tab. 2 show results for the randomized material variants. The selected distribution width parameters are the following:  $\eta_E = \eta_\nu = 0.95$  for H-R material and  $\eta_D = 0.8$  for H-RD and V-RD materials. It is seen that randomization of  $E_D$  does not change the means and variances, because deviatoric stiffness is not activated under the volumetric loading. Therefore, both H-RD and V-RD variants give results identical to deterministic models. This is true not only statistically but also locally, the results for elements within each RVE are identical to the deterministic models. The only difference is seen for the H-R variant, where both elastic modulus and Poisson's ratio are randomized. The mean values still converge to the mean values from deterministic variants with number of samples, however, the variances are much larger this time and cannot be decreased by improving convergence criteria. The stress solutions over the RVE are not constant but oscillate in space.

### 3.2. Deviatoric strain load

The RVEs are now subjected to purely deviatoric strain loads. The tensorial shear strains  $\varepsilon_{ij} = \gamma_{ij}/2$  where  $i \neq j$  are prescribed. In *Load 2* all the shear strains are equal to  $1.5 \times 10^{-5}$  and all normal strains are zero. In *Load 3* all strain components are zero except  $\varepsilon_{xy} = 1.5\sqrt{3} \times 10^{-5}$ . The deviatoric strain measure  $\varepsilon_{\text{eq}}$  computed equivalently to Von Mises stress is equal to  $4.5 \times 10^{-5}$  for both deviatoric loading scenarios. The stress tensors are studied in the original reference system  $xyz$  and their components denoted  $\sigma_{xx}$ ,  $\sigma_{yy}$ ,  $\sigma_{zz}$ ,  $\sigma_{yz}$ ,  $\sigma_{xz}$ , and  $\sigma_{xy}$ , but also in rotated reference system corresponding to principal directions of the macroscopic strain tensor where the components are denoted  $\sigma_{11}$ ,  $\sigma_{22}$ ,  $\sigma_{33}$ ,  $\sigma_{23}$ ,  $\sigma_{13}$ , and  $\sigma_{12}$ .

The H and V material variants produce a homogeneous stress field corresponding to the linearly elastic continuum by design in both loading scenarios. The standard material (S) and all the randomized materials

exhibit stress oscillations. Histograms of selected principal stress components under *Load 2* are shown in Fig. 2. The S material model is compared to H-R models with  $\eta_E = \eta_\nu = 0.7$ . This  $\eta$  choice produces  $\sigma_{22}$  stress oscillations in the H-R material similar to the S material, but  $\sigma_{33}$  and  $\sigma_{23}$  histograms are wider and narrower, respectively, than the corresponding histograms generated by S material.

For the comparison of the stress fields of the different materials, the  $\Delta_{\text{hist}}$  value is introduced. It measures the distance of two histograms of nodal stress components as Euclidian distance  $\Delta_{\text{hist}} = \pm \sqrt{\sum_{i=1}^n [h_1(i) - h_2(i)]^2}$  where  $h_1(i)$  and  $h_2(i)$  is the frequency of the  $i$ th bin in the first and the second histogram, respectively, and  $n$  is the number of bins, which is identical ( $n = 30$ ) in all histograms. The sign is added to indicate which distribution is wider and which is narrower. A negative sign means the peak of the first material (usually the S variant) is larger and vice versa. The  $\Delta_{\text{hist}}$  values of the histogram pairs from Fig. 2 are stated in the figure caption.

Firstly the RVEs of S and H-R materials were subjected to *Load 2*. The influence of the  $\eta_E$  and  $\eta_\nu$  governing randomization of the elastic parameters was inspected by measuring distance of stress histograms for S and H-R material. Figure 3 on the right-hand side shows that changing  $\eta_\nu$  at constant  $\eta_E = 0.7$  does not change the histogram distance, the histograms of all the components are insensitive to  $\eta_\nu$ . There is, however, strong sensitivity of them to  $\eta_E$ . This is seen in Fig. 3 on the left-hand side for constant  $\eta_\nu = 0.7$ . Lower values of  $\eta_E$  produce narrower histograms of stress components. Looking at the stress tensors in the  $xyz$  reference system (the top row in Fig. 3), one can conclude that for  $\eta_\nu = \eta_E = 0.7$ , the stress oscillations in H-R material closely resemble those in S material. Surprisingly, when transformed to the macroscopic principal directions, such an optimal value cannot be found as documented in the bottom row of Fig. 3. Also, the same random settings applied with *Load 3* do not lead to sufficient match, neither for  $xyz$  nor 123 reference system. All the histogram distances for  $\eta_\nu = \eta_E = 0.7$  are listed in Tab. 3.

The dependency of the H-R histograms on the chosen reference system is attributed to existing relations between stress tensor components. Table 4 shows Spearman (linear) correlation matrices of standard (S) and H-R material stress field components in reference systems  $xyz$ . The correlations for the standard material are negligible, while for H-R material they are significant. When some reference system transformation is applied, the almost independent standard material components transform differently from the H-R material, which exhibits significant dependencies. The correlations of stress field components were also inspected for an analogous continuum model. A periodic RVE with a similar number of nodes was constructed from three-dimensional trilinear isoparametric finite elements. The elastic parameters ( $E$  and  $\nu$ ) of the finite elements were randomized in the same fashion as in the H-R material and the resulting correlation matrices

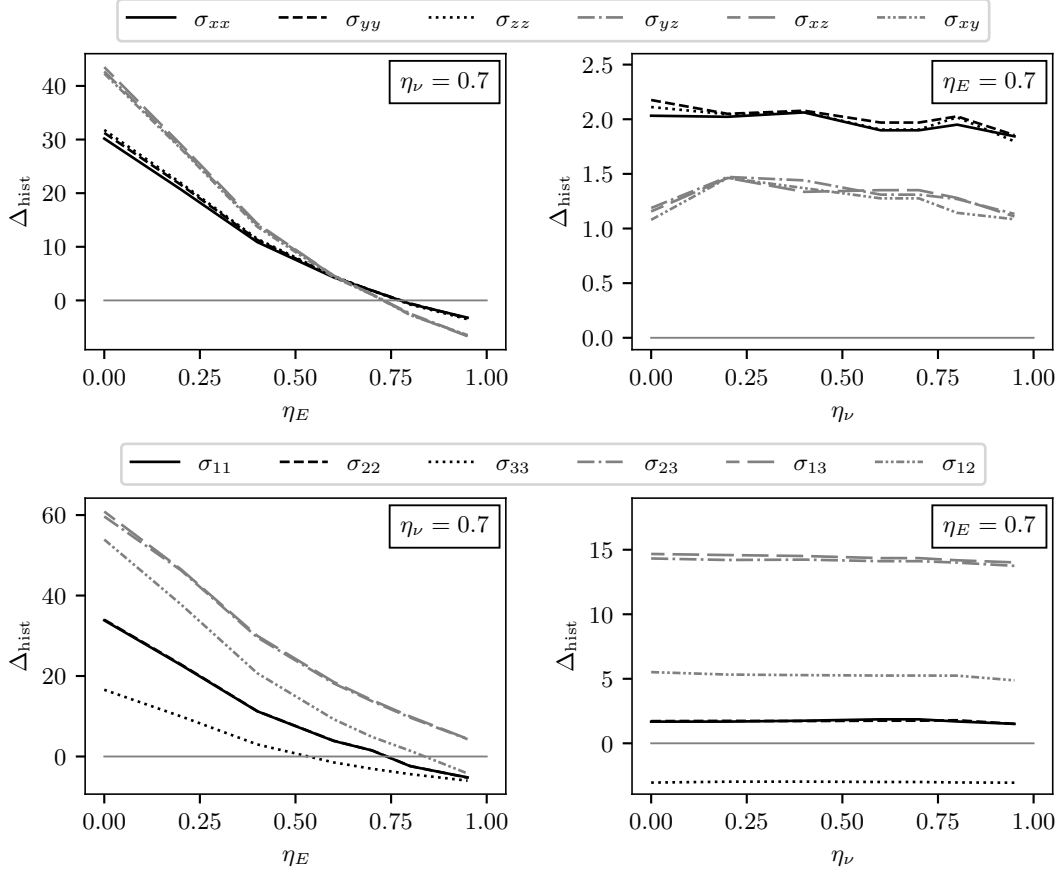


Figure 3: Histogram distance  $\Delta_{\text{hist}}$  between S and H-R material variants for different  $\eta_E$  and  $\eta_\nu$  parameters of randomization for *Load 2*. Top row: stress components in  $xyz$  reference system, bottom row: stress components in the reference system of principal strains, left column: fixed value  $\eta_\nu = 0.7$ , right column: fixed value  $\eta_E = 0.7$ .

reveal similar values as in the H-R material. The discrete H material behaves the same way as the continuous elastic model.

*Load 3* represents a different deviatoric load type. Attempts to minimize histogram distance  $\Delta_{\text{hist}}$  between H-R and S materials by changing  $\eta_E$  and  $\eta_\nu$  ended with unsatisfactory results for both  $xyz$  and 123 reference systems. The lowest values of  $\Delta_{\text{hist}}$  found can be seen in Tab. 3 as well. Randomizing the  $E$  and  $\nu$  parameters through  $E_D$  in H-RD material variant leads to similarly poor results as in the case of H-R material. On the left-hand side of Figure 4, it is shown that while it is once again possible to minimize the  $\Delta_{\text{hist}}$  for all components in the reference  $xyz$  system for the *Load 2*, the right-hand side shows that under *Load 3* no  $\eta_D$  value leads to oscillations matching those in the S material. Finally, the V-RD material variant produced another unsatisfactory result: there is no  $\eta_D$  value for which the histograms of all the stress components match those from the S material.

ref. system	load	$\sigma_{xx}$	$\sigma_{yy}$	$\sigma_{zz}$	$\sigma_{yz}$	$\sigma_{xz}$	$\sigma_{xy}$
coaxial, $xyz$	<i>Load 2</i>	2.062	2.078	2.065	1.440	1.336	1.370
	<i>Load 3</i>	1.852	1.722	-3.051	12.703	12.922	4.891
principal, 123	<i>Load 2</i>	1.751	1.723	-2.970	14.234	14.514	5.283
	<i>Load 3</i>	-3.312	-3.550	18.051	9.822	9.095	18.198

Table 3: Histogram distance  $\Delta_{\text{hist}}$  between S and H-R ( $\eta_E = \eta_\nu = 0.7$ ) material variants in coaxial and principal directions for *Load 2* and *Load 3*.

standard material (S)							homogenized randomized mat. (H-R)						
	$\sigma_{xx}$	$\sigma_{yy}$	$\sigma_{zz}$	$\sigma_{yz}$	$\sigma_{xz}$	$\sigma_{xy}$		$\sigma_{xx}$	$\sigma_{yy}$	$\sigma_{zz}$	$\sigma_{yz}$	$\sigma_{xz}$	$\sigma_{xy}$
$\sigma_{xx}$	1.0	-0.03	-0.04	-0.08	0.11	0.11	$\sigma_{xx}$	1.0	0.51	0.51	0.33	0.26	0.26
$\sigma_{yy}$	-0.03	1.0	-0.03	0.11	-0.08	0.11	$\sigma_{yy}$	0.51	1.0	0.51	0.26	0.33	0.26
$\sigma_{zz}$	-0.04	-0.03	1.0	0.11	0.11	-0.08	$\sigma_{zz}$	0.51	0.51	1.0	0.26	0.26	0.33
$\sigma_{yz}$	-0.08	0.11	0.11	1.0	0.17	0.17	$\sigma_{yz}$	0.33	0.26	0.26	1.0	0.55	0.55
$\sigma_{xz}$	0.11	-0.08	0.11	0.17	1.0	0.17	$\sigma_{xz}$	0.26	0.33	0.26	0.55	1.0	0.55
$\sigma_{xy}$	0.11	0.11	-0.08	0.17	0.17	1.0	$\sigma_{xy}$	0.26	0.26	0.33	0.55	0.55	1.0

Table 4: Correlations between components of the stress tensor in rigid bodies expressed in  $xyz$  reference system under *Load 2*; left: standard material (S); right: homogenized randomized material (H-R) with  $\eta_E = \eta_\nu = 0.7$ .

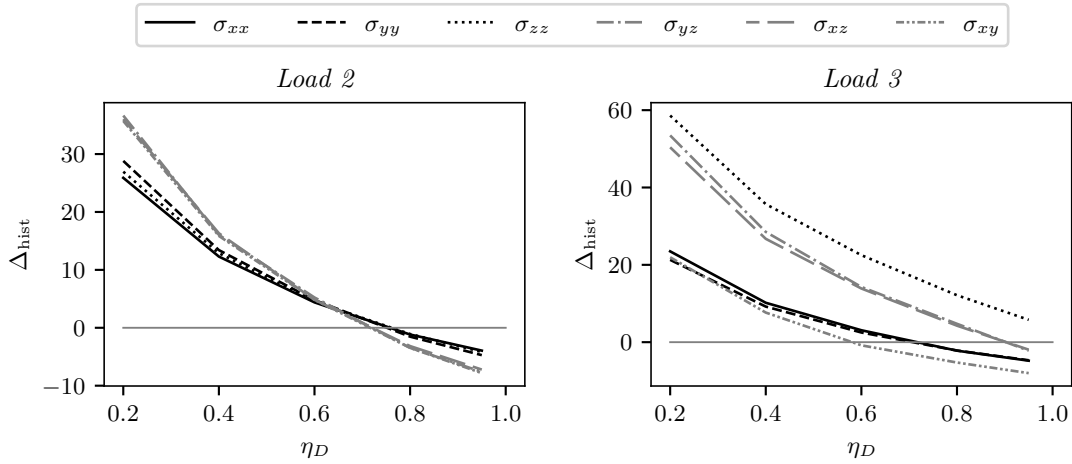


Figure 4: Histogram distance  $\Delta_{\text{hist}}$  between S and H-RD material variants for different  $\eta_D$  parameters of randomization for *Load 2* and *Load 3*

In the rest of this section, the H-RF material is studied and compared to S material in terms of variograms. The H-RF material, with both material parameters  $E$  and  $\nu$  ( $\eta_E = \eta_\nu = 0.7$ ) fluctuating according to realizations of two independent random fields, was subjected to *Load 2*. The variogram of  $\sigma_{xx}$  produced by the GSTools python package [38] is shown in Fig. 5 along with the best fits by a square exponential covariance model. It is seen that both H-R and V-RD material variants exhibit similar spatial dependency as the S material, but the H-RF material variant gives significantly lower variances. The H-RF variograms get closer to the other material variants with decreasing autocorrelation length  $\ell_c$ , however, there is a limit

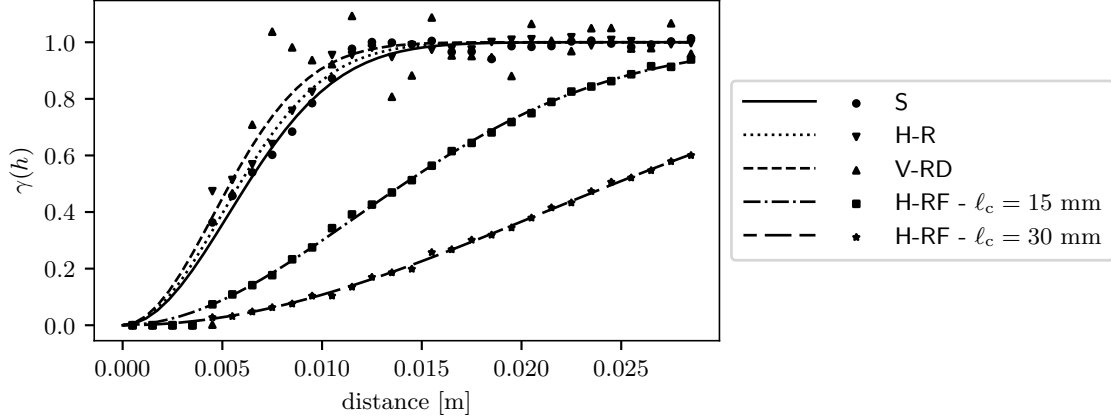


Figure 5: Variogram of  $\sigma_{xx}$  under *Load 2* for different autocorrelation lengths  $\ell_c$ .

given by the size of the rigid bodies under which the autocorrelation cannot be meaningfully represented. In the attempt to replicate the S material, the spatial correlation shall not be considered.

### 3.3. Combined deviatoric and volumetric load

Previously studied separately, the volumetric and deviatoric loads are now combined. Table 1 shows the macroscopic strain tensor defining *Load 4* as a sum of volumetric *Load 1* and deviatoric *Load 3*. Since the material is linearly elastic, the results are simply sum of the earlier results obtained for *Load 1* and *3*. Therefore, stress oscillations in S, H-RD, and V-RD material variants under *Load 4* are equal to those under *Load 3*, because the volumetric loading renders homogeneous stress field. On the contrary, H-R material variant sums two nonzero fields of oscillation. Once again it proves that no H-R randomization can replicate the standard material for varying loading vector since the volumetric component affects the stress oscillation differently.

Owing to the differing approaches to stress homogenization discussed earlier, the stress oscillations vary between the H-RD and V-RD materials, even when subjected to the same elastic parameter randomization and loads. In the case of *Load 3* and subsequently *Load 4* and randomization prescribed with  $\eta_D = 0.8$ , the standard deviation of the  $\sigma_{xx}$  component is higher for the H-RD compared to the V-RD ( $7.621 \times 10^4$  versus  $5.758 \times 10^4$ ). This trend holds for all other stress components, although the ratios of these values differ slightly between the stress components, as exemplified by the  $\sigma_{xz}$  component ( $3.266 \times 10^4$  versus  $2.905 \times 10^4$ ).

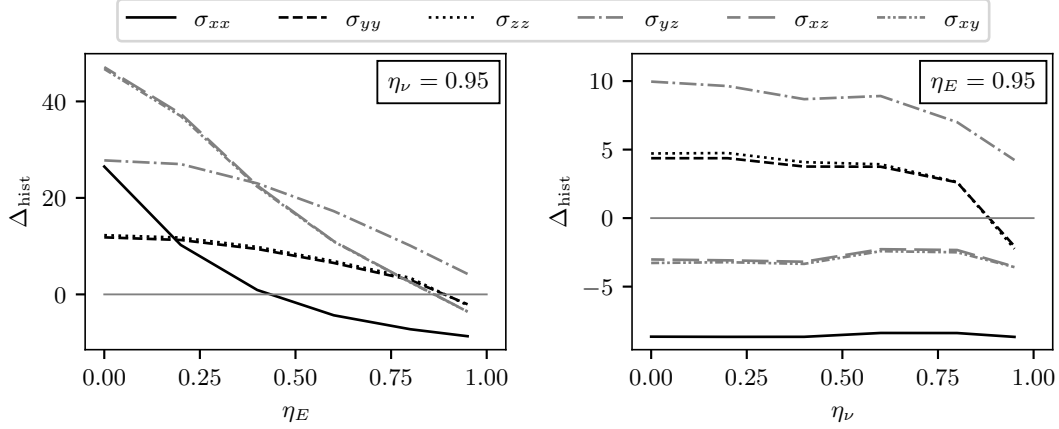


Figure 6: Histogram distance  $\Delta_{\text{hist}}$  between S and H-R material variants for different  $\eta_E$  and  $\eta_\nu$  parameters of randomization for *Load 5*. On the left at constant  $\eta_\nu = 0.95$ , on the right at constant  $\eta_E = 0.95$ .

#### 4. Inelastic behavior

The second portion of this research is devoted to the fracture behavior of the preceding models. The inelastic constitutive model described in Sec. 2.2 corresponds now to the standard material (S). The tensile strength  $f_t = 2.8 \text{ MPa}$  and fracture energy  $G_t = 40 \text{ J/m}^2$  are selected as typical values for structural concrete. The material variant H becomes the same inelastic material model extended by the projected eigenstrains according to Eq. (8), where the secant modulus  $(1 - d)E$  is substituted for elastic modulus  $E$ . In the elastic regime, the elastic H material is exactly recovered. Inelastic material behavior keeps its damage-based character as unloading occurs linearly toward the origin of the stress-strain space.

The periodic RVE is subjected to *Load 5*, an increasing macroscopic strain  $\varepsilon_{xx}$  while all shear strains are set to zero  $\gamma_{yz} = \gamma_{xz} = \gamma_{xy} = 0$  and transverse normal stresses are zero as well,  $\sigma_{yy} = \sigma_{zz} = 0$ . Figure 6 demonstrates that arguably the best fit for such loading, in terms of stress oscillation in elastic regime for H-R material, is  $\eta_E = \eta_\nu = 0.95$ . This analysis is identical to the one performed in Fig. 3 except the loading is different. Once again, it confirms randomization that at least partially resembles the standard material is dictated by the imposed load. Nevertheless, these  $\eta$  parameters are used hereinafter for the inelastic version of H-R material.

##### 4.1. S and H-R material variants

Figure 7 shows average stress  $\sigma_{xx}$  evolving with imposed strain  $\varepsilon_{xx}$ , computed on 100 RVEs of size  $l_{\text{RVE}} = 50 \text{ mm}$ . The smaller size was used for the sake of reducing computational time. On the left-hand side the average responses of the standard material (S), homogenized material (H), and two instances of

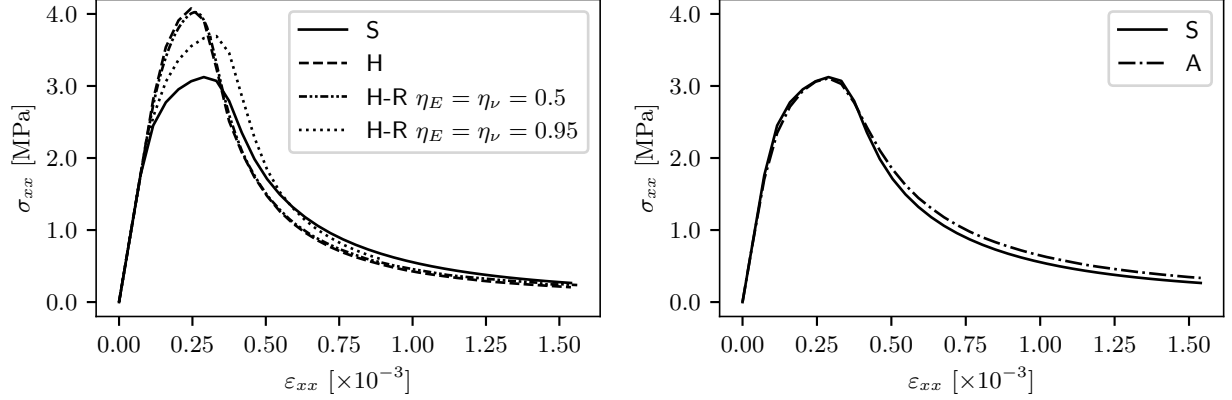


Figure 7: Stress-strain diagram computed as an average from 100 RVE responses to uniaxial strain loading; left: standard (S) material compared to homogenized (H) and randomized (H-R) variants; right: adjusted (A) material matching the standard one.

randomized material (H-R) are compared. The H material remains elastic longer as there is no randomness in the elastic phase. After attaining the peak load, however, the H material becomes more brittle as redistribution mechanisms due to heterogeneity are missing. Adding a moderate degree of randomness via  $\eta_\nu = \eta_E = 0.5$  does not improve correspondence much, even though earlier commencement of the inelastic phase, lower peak load, and slightly larger toughness are all apparent. For  $\eta_\nu = \eta_E = 0.95$  the difference is already substantial, but still far from the standard material. Since there is little margin for widening the uniform distribution (for  $\eta > 1$  negative values are reached), the fracture parameters of the H-R material are adjusted manually. By trial and error, it was found that the average response of the H-R material with  $\eta_\nu = \eta_E = 0.95$  and adjusted tensile strength to  $0.8f_t = 2.24$  MPa and fracture energy in tension to  $1.1G_t = 44$  J/m<sup>2</sup> matches closely the average response of the standard material. This optimally **adjusted** material variant will be designated as A hereinafter. The right side of Fig. 7 shows the matching mean responses of the S and A materials. Figure 8 shows stress-strain diagrams computed on larger RVE ( $l_{\text{RVE}} = 100$  mm) to verify that the described trends are independent of the RVE size. The same randomization of the elastic parameters and the same adjustments of the inelastic parameters are applied. While the shape of the diagrams is size dependent and therefore different from Fig. 7, the qualitative differences are preserved and the S and A materials still display similar responses.

Once the adjusted material (A) was created, we can study differences of its fracture process from the fracturing of the S material. Figure 9 shows the damage distribution in the RVE of size  $l_{\text{RVE}} = 100$  mm at the end of the simulation for the S, H, and A materials. All of them exhibit similar damage concentration in the macroscopic fracture region perpendicular to the loading direction. The H material displays less damage



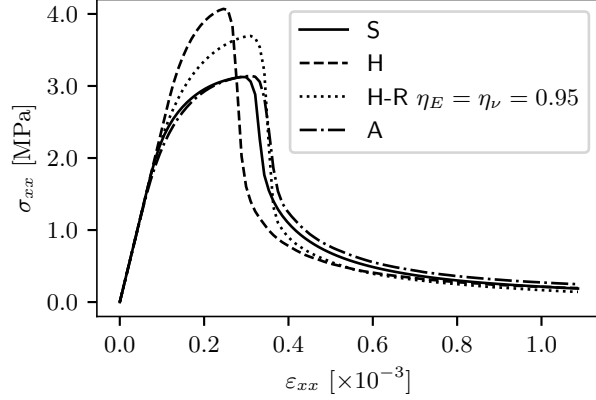


Figure 8: Stress strain-diagram of a single RVE of size  $l_{\text{RVE}} = 100$  mm subjected to *Load 5*.

outside the crack compared to the S and A materials. This is in agreement with the stress-strain diagram which indicates that both S and A materials undergo larger inelastic development prior to the peak stress at which the localization of strains into a macro-crack occurs.

The A material shows a similar amount of distributed damage as the S material; the hardening phase of both materials is also similar, as shown in Fig. 8. However, the character of the distributed damage differs. In the S material, the value of damage in an element is closely related to the orientation of the element with respect to the load direction. On the contrary, Fig. 10 demonstrates that the relationship between damage in the A material and the element orientation is weakened, both at peak load and when approaching a traction-free crack condition. In the four histograms in Fig. 10, the distance from the center corresponds to the element damage value and the angular distance from horizontal direction is the angle  $\varphi$  between element normal direction,  $\mathbf{n}_N$ , and loading direction along  $x$  axis. This domain is divided into bins and the depth of the blue color indicates number of elements in the bins over 30 RVE simulations. At peak load, there are no elements fully damaged and almost no partially damaged elements with  $\varphi > 70^\circ$ . The S material exhibits a narrow range of damage dependent on element orientation. The A material follows this dependence, but the range is significantly larger. At the end of simulations, as the models approach the traction-free crack condition, one can see a large number of elements with damage value close to 1. These elements are associated with the macroscopic crack.

#### 4.2. H-RF material variant

The previous inelastic simulations considered only the spatially independent randomization of elastic parameters. To study the effect of the spatial correlation of the elastic parameters on the inelastic response, random fields of several correlation lengths,  $\ell_c$ , were generated and applied in the H-RF material variant.

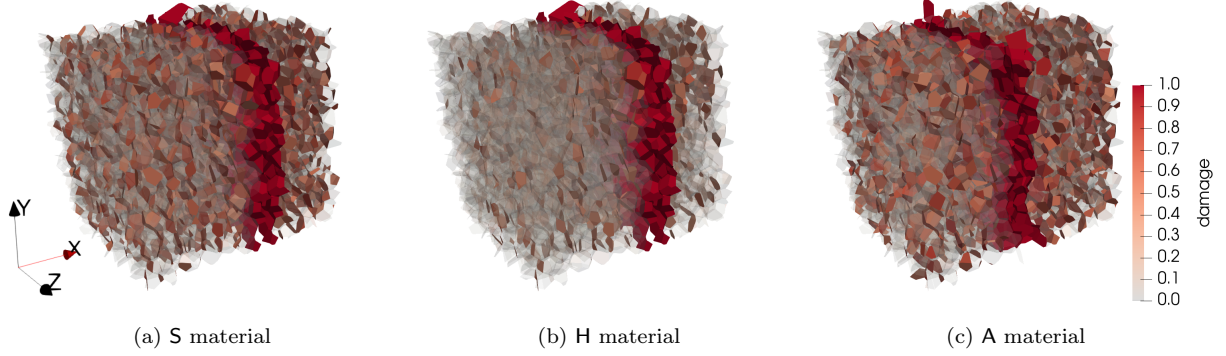


Figure 9: Damage distribution in RVEs at the end of tensile loading from Fig. 8, loading direction is along the  $x$  axis.

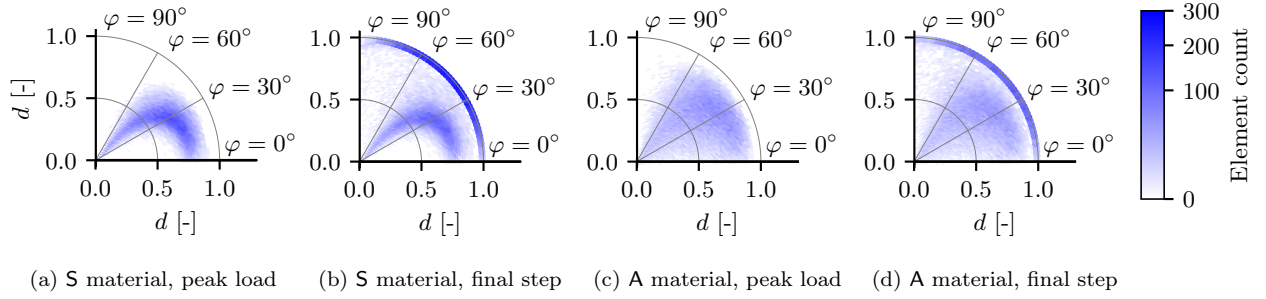


Figure 10: Two dimensional histograms where distance from the center indicates damage variable and angle  $\varphi$  is formed by the element normal and the loading direction.

The maximum stress  $\max(\sigma_{xx})$  and dissipated energy  $E_{\text{dis}}$  are computed for  $\ell_c$  between 7 mm and 50 mm on RVEs of size  $l_{\text{RVE}} = 100$  mm. Following from the preceding section, the same adjustments are made to the tensile strength and fracture energy in tension:  $f_t = 2.24$  MPa and  $G_t = 44$  J/m<sup>2</sup>. The probability distribution is still uniform with  $\eta_\nu = \eta_E = 0.95$ .

Figure 11 shows mean values and bands of  $\pm$  one standard deviation of  $\max(\sigma_{xx})$  and  $E_{\text{dis}}$  based on 100 simulations. The results closely resemble results obtained and interpreted in Refs. [19, 49], in which the randomized variables were local strength and fracture energy. There is a minimum value of macroscopic strength appearing at a critical correlation length. This length is long enough so the stress fluctuations are not *averaged* out within the fracture process zone, but also short enough so the *weakest link* effect can take place. For longer correlation lengths the weakest link model is gradually suppressed so the strength increases. Asymptotically, the material behavior approaches behavior of a random but spatially constant material. Variability of strength increases with  $\ell_c$  as well because the averaging within the fracture process zone is reduced and the weakest link effect diminishes. For shorter  $\ell_c$  the averaging within the fracture process

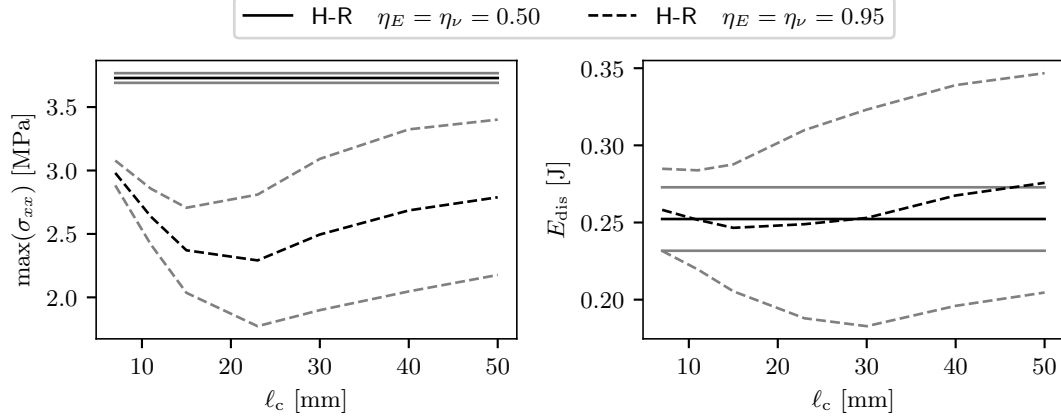


Figure 11: Maximum stress  $\max(\sigma_{xx})$  and dissipated energy  $E_{\text{dis}}$ , mean and band of  $\pm$  one standard deviation for varying  $\ell_c$ .

zone reduces apparent material variability and therefore strength increases while its variability diminishes. In an extreme case of  $\ell_c \rightarrow 0$  the response of the H-RF material should approach the H-R response, but the discretization into finite size rigid bodies prevents usage of random fields with  $\ell_c$  below 7 mm.

Similar effects can be seen also for dissipated energy. There is a critical correlation length for which the dissipation is minimized. Also the standard deviation grows with  $\ell_c$ . Both of these effects are milder than what was seen for strength. Since the tensile fracture energy at the contacts is constant, the observed behavior must be attributed to different fracture character. At the critical  $\ell_c$ , the macroscopic crack is thought to be the most localized so the energy dissipation is the lowest.

## 5. Conclusions

The stress oscillations in discrete models with *non-physical* discretization are controlled by (i) homogenizing the local response of the discrete structure and subsequently (ii) introducing a controlled degree of randomness via the assignment of elastic material parameters in space. Such stress oscillations are of special interest as they influence (and in some situations govern) fracture behavior. Two means for homogenizing the local behavior (i.e., the volumetric-deviatoric decomposition of the constitutive model and the auxiliary stress projection method) are implemented, rendering essentially identical elastically homogeneous materials. Several randomization techniques are introduced and compared. None of them is found to be capable of reconstructing the character of the stress oscillations present in discrete models based on *physical* discretizations of material structure and standard constitutive relations.

The following conclusions are drawn based on a large number of numerical simulations performed on

periodic discrete structures. For the elastic regime the particular conclusions read:

- For a pure volumetric loading both the standard and homogenized materials produce homogeneous stress fields. As expected, spatial randomization of macroscopic elastic modulus and Poisson's ratio parameters leads to inhomogeneous stress fields. However, randomizing only the deviatoric part of the constitutive model preserves the homogeneous stresses.
- There appears to be no method for randomizing the elasticity parameters of the homogenized material that recovers the statistical characteristics of stress field exhibited by the standard material model for all loading scenarios. The randomization that matches the standard material depends on the imposed load.
- Moreover, randomization that produces reasonably matching stress fields may not exist for a particular loading scenario. Firstly, it might be impossible to match distributions of all the tensorial stress components for the standard and randomized materials. Secondly, the standard material model generates statistically independent stress components while the randomized material exhibits significant correlations between them. Consequently, rotation of the reference system changes the stress components in these materials differently.
- When the same randomization is applied to the homogenized materials with the volumetric-deviatoric decomposition and with the auxiliary stress projection, the latter one gives stress oscillations with a smaller variability. These materials differ only in the way the randomization propagates through the model, otherwise, they should be considered identical.
- The spatial correlation of the stress field produced by the standard material is best reproduced by randomizing the elastic parameters of each discrete contact independently. When using spatial dependence in the form of a random field with correlation length larger or equal to the size of rigid bodies, the resulting correlation lengths of the stress tensor components are substantially larger compared to those of the standard material.

Several additional conclusions can be drawn regarding the fracture behavior of these models:

- Because the homogenized material effectively eliminates all the heterogeneity in the elastic regime, it enters the inelastic domain at larger strains than the standard material. Furthermore, its strength is larger and the softening phase is steeper.

- Randomization of elastic material properties of the homogenized material introduces heterogeneity and therefore leads to earlier start of inelastic effects, lower strength and milder slope of the softening phase. Nevertheless, even large variability in elastic parameters does not introduce sufficient heterogeneity to reproduce the macroscopic behavior of the standard material.
- The fracture parameters of the homogenized material with randomized elasticity can be adjusted so its inelastic response matches the response of the standard material. Even then there are significant differences in terms of orientations of the damaged contacts before the macroscopic crack appears. Damage in the standard material is closely associated with contact orientation, while the homogenized material weakens this relation.
- When the elastic parameters are randomized with spatial correlation, there is a critical correlation length for which the strength is minimal. This pattern corresponds to a behavior previously observed in Ref. [21] explained by a combination of the weakest link effect and the averaging of stress within the fracture process zone. This time, a milder but essentially identical effect is seen also for energy dissipation, which is also minimized around the critical correlation length.

The elastic and fracture behaviors of several variants of randomized homogeneous models have been examined herein, using a standard constitutive model with physically-based discretization as a comparator. Based on the simulations, one cannot conclude which model is more realistic. Benchmark comparisons using appropriate physical test results seem necessary to inform and help guide future research efforts.

## Acknowledgement

Jan Eliáš and Jan Raisinger acknowledge financial support provided by the Czech Ministry of Education, Youth and Sports under project No. LUAUS24260 and by project INODIN (Innovative methods of materials diagnostics and monitoring of engineering infrastructure to increase its durability and service time – CZ.02.01.01/00/23\_020/0008487) co-funded by European Union. The former project financed the development of the homogenization technique and implementation of the RVE model, the latter was used to implement other material models and conduct the statistical study. For the purpose of Open Access, a CC BY 4.0 public copyright licence has been applied by the authors to the present document and will be applied to all subsequent versions up to the Author Accepted Manuscript arising from this submission.

## Data availability

Computational models, scripts to run them, and their results are available at Zenodo repository under DOI 10.5281/zenodo.15303637.

## References

- [1] M. Alnaggar, D. Pelessone, and G. Cusatis. “Lattice Discrete Particle Modeling of Reinforced Concrete Flexural Behavior”. In: *Journal of Structural Engineering* 145.1 (2019), p. 04018231. DOI: 10.1061/(ASCE)ST.1943-541X.0002230.
- [2] D. Asahina et al. “Elastically-homogeneous lattice models of damage in geomaterials”. In: *Computers and Geotechnics* 81 (Jan. 2017), pp. 195–206. DOI: 10.1016/j.compgeo.2016.08.015.
- [3] D. Asahina et al. “Simulating the Poisson effect in lattice models of elastic continua”. In: *Computers and Geotechnics* 70 (2015), pp. 60–67. ISSN: 0266-352X. DOI: 10.1016/j.compgeo.2015.07.013.
- [4] K. Bagi. “Stress and strain in granular assemblies”. In: *Mechanics of Materials* 22.3 (1996), pp. 165–177. ISSN: 0167-6636. DOI: 10.1016/0167-6636(95)00044-5.
- [5] J. Bathurst R. and Rothenburg L. “Micromechanical Aspects of Isotropic Granular Assemblies With Linear Contact Interactions”. In: *Journal of Applied Mechanics* 55.1 (1988), pp. 17–23. ISSN: 0021-8936. DOI: 10.1115/1.3173626.
- [6] Z. P. Bažant et al. “Random Particle Model for Fracture of Aggregate or Fiber Composites”. In: *Journal of Engineering Mechanics* 116.8 (1990), pp. 1686–1705. DOI: 10.1061/(ASCE)0733-9399(1990)116:8(1686).
- [7] T. Bhaduri, S. Gomaa, and M. Alnaggar. “Coupled Experimental and Computational Investigation of the Interplay between Discrete and Continuous Reinforcement in Ultrahigh Performance Concrete Beams. II: Mesoscale Modeling”. In: *Journal of Engineering Mechanics* 147.9 (2021), p. 04021050. DOI: 10.1061/(ASCE)EM.1943-7889.0001941.
- [8] J. E. Bolander et al. “Discrete mechanical models of concrete fracture”. In: *Engineering Fracture Mechanics* 257 (2021), p. 108030. ISSN: 0013-7944. DOI: 10.1016/j.engfracmech.2021.108030.
- [9] J.E. Bolander and S. Saito. “Fracture analyses using spring networks with random geometry”. In: *Engineering Fracture Mechanics* 61.5 (1998), pp. 569–591. ISSN: 0013-7944. DOI: 10.1016/S0013-7944(98)00069-1.

- [10] G. Cusatis and L. Cedolin. “Two-scale study of concrete fracturing behavior”. In: *Engineering Fracture Mechanics* 74.1 (2007). Fracture of Concrete Materials and Structures, pp. 3–17. ISSN: 0013-7944. DOI: 10.1016/j.engfracmech.2006.01.021.
- [11] G. Cusatis, D. Pelessone, and A. Mencarelli. “Lattice Discrete Particle Model (LDPM) for failure behavior of concrete. I: Theory”. In: *Cement and Concrete Composites* 33.9 (2011), pp. 881–890. ISSN: 0958-9465. DOI: 10.1016/j.cemconcomp.2011.02.011.
- [12] G. Cusatis, R. Rezakhani, and E. A. Schaufert. “Discontinuous Cell Method (DCM) for the simulation of cohesive fracture and fragmentation of continuous media”. In: *Engineering Fracture Mechanics* 170 (2017), pp. 1–22. ISSN: 0013-7944. DOI: 10.1016/j.engfracmech.2016.11.026.
- [13] A. Drescher and G. de Josselin de Jong. “Photoelastic verification of a mechanical model for the flow of a granular material”. In: *Journal of the Mechanics and Physics of Solids* 20.5 (1972), pp. 337–340. ISSN: 0022-5096. DOI: 10.1016/0022-5096(72)90029-4.
- [14] J. Eliáš. “Adaptive technique for discrete models of fracture”. In: *International Journal of Solids and Structures* 100–101 (2016), pp. 376–387. ISSN: 0020-7683. DOI: 10.1016/j.ijsolstr.2016.09.008.
- [15] J. Eliáš. “Boundary Layer Effect on Behavior of Discrete Models”. In: *Materials* 10 (2017), p. 157. ISSN: 1996-1944. DOI: 10.3390/ma10020157.
- [16] J. Eliáš. “Elastic properties of isotropic discrete systems: Connections between geometric structure and Poisson’s ratio”. In: *International Journal of Solids and Structures* 191-192 (2020), pp. 254–263. ISSN: 0020-7683. DOI: 10.1016/j.ijsolstr.2019.12.012.
- [17] J. Eliáš and G. Cusatis. “Homogenization of discrete mesoscale model of concrete for coupled mass transport and mechanics by asymptotic expansion”. In: *Journal of the Mechanics and Physics of Solids* 167 (2022), p. 105010. ISSN: 0022-5096. DOI: 10.1016/j.jmps.2022.105010.
- [18] J. Eliáš and G. Cusatis. “Macroscopic stress, couple stress and flux tensors derived through energetic equivalence from microscopic continuous and discrete heterogeneous finite representative volumes”. In: *Computer Methods in Applied Mechanics and Engineering* 436 (2025), p. 117688. ISSN: 0045-7825. DOI: 10.1016/j.cma.2024.117688.
- [19] J. Eliáš and M. Vořechovský. “Fracture in random quasibrittle media: I. Discrete mesoscale simulations of load capacity and fracture process zone”. In: *Engineering Fracture Mechanics* 235 (2020), p. 107160. ISSN: 0013-7944. DOI: 10.1016/j.engfracmech.2020.107160.

- [20] J. Eliáš and M. Vořechovský. “Modification of the Audze–Eglajs criterion to achieve a uniform distribution of sampling points”. In: *Advances in Engineering Software* 100 (2016), pp. 82–96. ISSN: 0965-9978. DOI: 10.1016/j.advengsoft.2016.07.004.
- [21] J. Eliáš, M. Vořechovský, and V. Sadílek. “Periodic version of the minimax distance criterion for Monte Carlo integration”. In: *Advances in Engineering Software* 149 (2020), p. 102900. ISSN: 0965-9978. DOI: 10.1016/j.advengsoft.2020.102900.
- [22] J. Eliáš et al. “Stochastic discrete meso-scale simulations of concrete fracture: comparison to experimental data”. In: *Engineering Fracture Mechanics* 135 (2015), pp. 1–16. ISSN: 0013-7944. DOI: 10.1016/j.engfracmech.2015.01.004.
- [23] R. G. Ghanem and P. D. Spanos. *Stochastic finite elements: a spectral approach*. Courier Corporation, 2003.
- [24] P. Grassl. “3D lattice meso-scale modelling of the effect of lateral compression on tensile fracture processes in concrete”. In: *International Journal of Solids and Structures* 262-263 (2023), p. 112086. ISSN: 0020-7683. DOI: 10.1016/j.ijsolstr.2022.112086.
- [25] D. Jia, J. C. Brigham, and A. Fascetti. “An efficient static solver for the Lattice Discrete Particle Model”. In: *Computer-Aided Civil and Infrastructure Engineering* 39.23 (2024), pp. 3531–3551. DOI: 10.1111/mice.13306.
- [26] J. Kang and J. E. Bolander. “Event-based lattice modeling of strain-hardening cementitious composites”. In: *International Journal of Fracture* 206 (2017), pp. 245–261.
- [27] K. Karhunen. *Zur Spektraltheorie stochastischer Prozesse*. Annales Academiae scientiarum Fennicae. 1946.
- [28] A. Kikuchi, T. Kawai, and N. Suzuki. “The rigid bodies—spring models and their applications to three-dimensional crack problems”. In: *Computers & Structures* 44.1 (1992), pp. 469–480. ISSN: 0045-7949. DOI: 10.1016/0045-7949(92)90269-6.
- [29] N. P. Kruyt and L. Rothenburg. “Micromechanical Definition of the Strain Tensor for Granular Materials”. In: *Journal of Applied Mechanics* 63.3 (Sept. 1996), pp. 706–711. ISSN: 0021-8936. DOI: 10.1115/1.2823353.
- [30] E. Kuhl et al. “A comparison of discrete granular material models with continuous microplane formulations”. In: *Granular Matter* 2.3 (2000), pp. 113–121. ISSN: 1434-5021. DOI: 10.1007/s100350050003.



- [31] Ch. Li and A. Der Kiureghian. “Optimal Discretization of Random Fields”. In: *J Eng Mech - ASCE* 119.6 (1993), pp. 1136–1154. ISSN: 0733-9399. DOI: 10.1061/(ASCE)0733-9399(1993)119:6(1136).
- [32] H. Li, Z. Lü, and X. Yuan. “Nataf transformation based point estimate method”. In: *Chin Sci Bull* 53.17 (2008), pp. 2586–2592. DOI: 10.1007/s11434-008-0351-0.
- [33] A. E. H. Love. *A treatise on the mathematical theory of elasticity*. Vol. 1. Cambridge University Press, 1927.
- [34] J. Luo, S. Asamoto, and K. Nagai. “Mesoscale simulation of compression-induced cracking and failure of ASR-damaged concrete with stirrup confinement”. In: *Engineering Fracture Mechanics* 277 (2023), p. 108977. ISSN: 0013-7944. DOI: 10.1016/j.engfracmech.2022.108977.
- [35] J. Mašek, J. Květoň, and J. Eliáš. “Adaptive discretization refinement for discrete models of coupled mechanics and mass transport in concrete”. In: *Construction and Building Materials* 395 (2023), p. 132243. ISSN: 0950-0618. DOI: 10.1016/j.conbuildmat.2023.132243.
- [36] Taito Miura, Hikaru Nakamura, and Yoshihito Yamamoto. “Expansive spalling mechanism of concrete due to high temperature based on developed hygro-thermal-mechanical model by 3D-RBSM-TNM”. In: *Engineering Fracture Mechanics* 284 (2023), p. 109216. ISSN: 0013-7944. DOI: 10.1016/j.engfracmech.2023.109216.
- [37] Francisco Montero-Chacón, Héctor Cifuentes, and Fernando Medina. “Fracture analyses using spring networks with random geometry”. In: *Materials* 10.2 (2017), p. 207. ISSN: 1996-1944. DOI: 10.3390/ma10020207.
- [38] S. Müller et al. “GSTools v1.3: a toolbox for geostatistical modelling in Python”. In: *Geoscientific Model Development* 15.7 (2022), pp. 3161–3182. DOI: 10.5194/gmd-15-3161-2022.
- [39] K. Nagai, Y. Sato, and T. Ueda. “Mesoscopic simulation of failure of mortar and concrete by 3D RBSM”. In: *Journal of Advanced Concrete Technology* 3.3 (2005), pp. 385–402.
- [40] F. Nicot et al. “On the definition of the stress tensor in granular media”. In: *International Journal of Solids and Structures* 50.14 (2013), pp. 2508–2517. ISSN: 0020-7683. DOI: 10.1016/j.ijsolstr.2013.04.001.
- [41] A. Okabe et al. *Spatial Tessellations: Concepts and Applications of Voronoi Diagrams*. Vol. 43. Jan. 2000. ISBN: 9780471986355. DOI: 10.2307/2687299.

- [42] R. Rezakhani and G. Cusatis. “Asymptotic expansion homogenization of discrete fine-scale models with rotational degrees of freedom for the simulation of quasi-brittle materials”. In: *Journal of the Mechanics and Physics of Solids* 88 (2016), pp. 320–345. ISSN: 0022-5096. DOI: 10.1016/j.jmps.2016.01.001.
- [43] R. Rezakhani, X. Zhou, and G. Cusatis. “Adaptive multiscale homogenization of the lattice discrete particle model for the analysis of damage and fracture in concrete”. In: *International Journal of Solids and Structures* 125 (2017), pp. 50–67. ISSN: 0020-7683. DOI: h10.1016/j.ijsolstr.2017.07.016.
- [44] E. Schlangen and E.J. Garboczi. “Fracture simulations of concrete using lattice models: Computational aspects”. In: *Engineering Fracture Mechanics* 57.2 (1997), pp. 319–332. ISSN: 0013-7944. DOI: 10.1016/S0013-7944(97)00010-6.
- [45] E. Schlangen and J.G.M. van Mier. “Simple lattice model for numerical simulation of fracture of concrete materials and structures”. In: *Materials and Structures* 25 (1992), pp. 534–542. ISSN: 1359–5997. DOI: 10.1007/BF02472449.
- [46] P. D. Spanos and R. G. Ghanem. “Stochastic finite element expansion for random media”. In: *J. Eng. Mech., ASCE* 115.5 (1989), pp. 1035–1053.
- [47] G. Stefanou. “The stochastic finite element method: Past, present and future”. In: *Comp. Meth. Appl. Mech. Eng.* 198.2009 (2009), pp. 1031–1051.
- [48] M. Vořechovský. “Simulation of simply cross correlated random fields by series expansion methods”. In: *Struct Saf* 30.4 (2008), pp. 337–363. ISSN: 0167-4730. DOI: 10.1016/j.strusafe.2007.05.002.
- [49] M. Vořechovský and J. Eliáš. “Fracture in random quasibrittle media: II. Analytical model based on extremes of the averaging process”. In: *Engineering Fracture Mechanics* 235 (2020), p. 107155. ISSN: 0013-7944. DOI: 10.1016/j.engfracmech.2020.107155.
- [50] M. Vořechovský and J. Eliáš. “Modification of the Maximin and  $\phi_p$  (phi) criteria to achieve statistically uniform distribution of sampling points”. In: *Technometrics* 62.3 (2020), pp. 371–386. ISSN: 0040-1706. DOI: 10.1080/00401706.2019.1639550.
- [51] M. Vořechovský and D. Novák. “Correlation control in small-sample Monte Carlo type simulations I: A simulated annealing approach”. In: *Probabilist Eng Mech* 24.3 (2009), pp. 452–462. ISSN: 0266-8920. DOI: 10.1016/j.probengmech.2009.01.004.
- [52] J. Weber. “Recherches concernant les contraintes intergranulaires dans les milieux pulvérulents”. In: *Bulletin de Liaison des Ponts-et-Chaussées* 20 (1966), pp. 1–20.

- [53] B. Yan and R. A. Regueiro. “Definition and symmetry of averaged stress tensor in granular media and its 3D DEM inspection under static and dynamic conditions”. In: *International Journal of Solids and Structures* 161 (2019), pp. 243–266. ISSN: 0020-7683. DOI: 10.1016/j.ijsolstr.2018.11.021.
- [54] L. Yang et al. “A novel analytical model of particle size distributions in granular materials”. In: *Engineering with Computers* (2024). ISSN: 1435-5663. DOI: 10.1007/s00366-024-02042-7.
- [55] H. Yin et al. “An interprocess communication-based two-way coupling approach for implicit–explicit multiphysics lattice discrete particle model simulations”. In: *Engineering Fracture Mechanics* 310 (2024), p. 110515. ISSN: 0013-7944. DOI: 10.1016/j.engfracmech.2024.110515.
- [56] Q. Zhang et al. “Discrete Modeling of Elastic Heterogeneous Media”. In: *Mechanics Research Communications* 137 (2024), p. 104277. ISSN: 0093-6413. DOI: 10.1016/j.mechrescom.2024.104277.
- [57] Y. Zhou et al. “A lattice modelling framework for fracture-induced acoustic emission wave propagation in concrete”. In: *Engineering Fracture Mechanics* 312 (2024), p. 110589. ISSN: 0013-7944. DOI: 10.1016/j.engfracmech.2024.110589.
- [58] Z. Zhu et al. “Lattice discrete particle modeling of concrete under cyclic tension–compression with multi-axial confinement”. In: *Construction and Building Materials* 352 (2022), p. 128985. ISSN: 0950-0618. DOI: 10.1016/j.conbuildmat.2022.128985.